Passive metamaterial-based acoustic holograms in ultrasound energy transfer systems

Marjan Bakhtiari-Nejad, Ahmed Elnahhas, Muhammad R. Hajj, Shima Shahab

Marjan Bakhtiari-Nejad, Ahmed Elnahhas, Muhammad R. Hajj, Shima Shahab, "Passive metamaterial-based acoustic holograms in ultrasound energy transfer systems," Proc. SPIE 10595, Active and Passive Smart Structures and Integrated Systems XII, 1059518 (15 March 2018); doi: 10.1117/12.2296741

SPIE.

Event: SPIE Smart Structures and Materials + Nondestructive Evaluation and Health Monitoring, 2018, Denver, Colorado, United States

Passive metamaterial-based acoustic holograms in ultrasound energy transfer systems

Marjan Bakhtiari-Nejad*[a], Ahmed Elnahhas[b], Muhammad R. Hajj[a] and Shima Shahab[a]

[a]Department of Biomedical Engineering and Mechanics, Virginia Polytechnic Institute and State University, Blacksburg, VA 24061, USA

[b]Department of Mechanical Engineering, Virginia Polytechnic Institute and State University, Blacksburg, VA 24061, USA

ABSTRACT

Contactless energy transfer (CET) is a technology that is particularly relevant in applications where wired electrical contact is dangerous or impractical. Furthermore, it would enhance the development, use, and reliability of low-power sensors in applications where changing batteries is not practical or may not be a viable option. One CET method that has recently attracted interest is the ultrasonic acoustic energy transfer, which is based on the reception of acoustic waves at ultrasonic frequencies by a piezoelectric receiver. Patterning and focusing the transmitted acoustic energy in space is one of the challenges for enhancing the power transmission and locally charging sensors or devices. We use a mathematically designed passive metamaterial-based acoustic hologram to selectively power an array of piezoelectric receivers using an unfocused transmitter. The acoustic hologram is employed to create a multifocal pressure pattern in the target plane where the receivers are located inside focal regions. We conduct multiphysics simulations in which a single transmitter is used to power multiple receivers with an arbitrary two-dimensional spatial pattern via wave controlling and manipulation, using the hologram. We show that the multi-focal pressure pattern created by the passive acoustic hologram will enhance the power transmission for most receivers.

Keywords: Acoustic hologram, metamaterial, contactless power transfer, ultrasonic acoustic energy transfer

1. INTRODUCTION

Ultrasonic acoustic energy transfer (UAET) has emerged as a new approach for contactless energy transfer (CET). UAET relies on transferring energy using sound waves and is primarily implemented using piezoelectric (PZT) transmitters and receivers. Several proof-of-concept experiments have been conducted through different media reporting various efficiencies, and a review highlighting major advancements is presented by Roes *et al.* [1]. One of the challenges for enhancing the wireless power transmission and selectively charging sensors or devices is patterning and focusing the transmitted acoustic energy in space. The localization of energy is important as it can be used for biomedical applications such as lithotripsy [2] (kidney stone removal), or more general applications such as powering sensor networks efficiently. Furthermore, there are scenarios where localizing the energy transfer is not only a desire but a must due to the delicacy of the system in which energy transfer is implemented. Such examples include sensor nodes [3] or neural dust sensing motes placed throughout the human brain [4]. One scenario is the use of high-intensity focused ultrasound (HIFU) technology [5] or acoustic mirroring concept [6-8] to focus the transmitted energy in space, and, thereby, strongly excite the receiver. However, focusing should obviously be employed in UAET with care since HIFU may yield substantial energy localization and heating [5]. Safety regulations require acoustic intensity that is lower than 94 mW/cm^2 and limit the operating frequency to 100 kHz [9]. In this research, for the first time, we employ the capabilities of a metamaterial-based acoustic hologram in beam steering and multi-focal lensing for contactless acoustic power transfer.

* marjanbn@vt.edu; phone 1 540 231 8789; www.beam.vt.edu

Active and Passive Smart Structures and Integrated Systems XII, edited by Alper Erturk, Jae-Hung Han,
Proc. of SPIE Vol. 10595, 1059518 · © 2018 SPIE · CCC code: 0277-786X/18/$18 · doi: 10.1117/12.2296741

Acoustic holographic techniques are used in applications where spatial reconstruction and/or control of acoustic pressure fields is required. The hologram stores the phase and amplitude profile of a desired wave front, which is used to reconstruct the acoustic pressure fields depending on the desired application [10]. The storage of the wavefront information in an acoustic hologram is achieved by utilizing metamaterials [11]. Although these techniques were first applied to optical holograms, their acoustic analogues have been developed by multiple research groups. Recently, Melde *et al.* [10] and Xie *et al.* [11] investigated acoustic holograms that needed only one coherent acoustic source for reproduction. This was a substantial contribution to the field of acoustic holography due to the simplification of the process, where acoustic holograms initially were designed using complex phased arrays of transducers with the need for phase-shifting circuits [12]. By replacing the active phased arrays with a single source and a holographic lens that stores the desired wavefront information, acoustic holograms operate similarly to their optical counterparts.

We propose to combine UAET systems with the diffraction-limited acoustic holograms employing the customized fabrication procedure that was first presented by Melde *et al.* [10]. We utilize an iterative angular spectrum approach (IASA) [13] to create the desired acoustic pressure patterns for the hologram fabrication. The output pressure pattern is then used in conjunction with a distributed parameter piezoelectric model [6, 14] to compute the power output from a distribution of 33-mode receivers. Figure 1 displays a schematic of our proposed system, which includes an array of piezoelectric receivers (shunted to an electrical load) that are located in a target plane, excited by incident acoustic waves originating from a cylindrical acoustic source (transmitter) and are modulated (shaped) by an acoustic hologram. We use this setup to investigate the capability of combining UAET and acoustic holography techniques for focusing and patterning the transmitted energy in space as well as enhancing the power output from the receivers located at specific focal points. In future setups, a third domain will be introduced to minimize possible impedance mismatch at the surfaces of the transmitter, hologram and receivers.

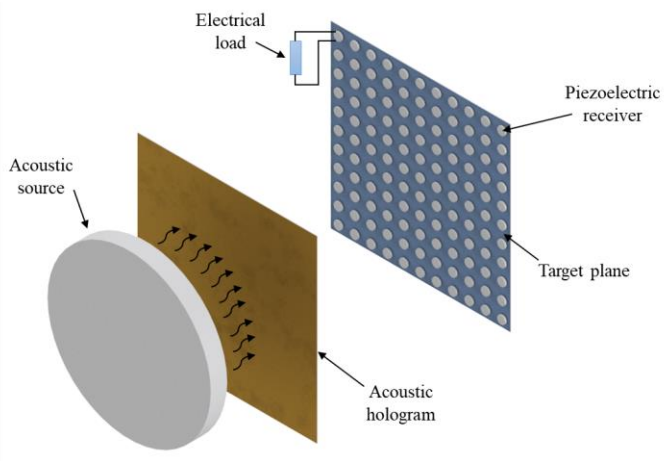

Figure 1. Schematic representation of implementing an acoustic hologram in an ultrasound energy transfer system. The PZT receivers are located in a target plane (each receiver's axis of symmetry is perpendicular to the target plane)

2. THEORY

2.1. Wave propagation and acoustic pressure from transmitter and hologram

The acoustic pressure close to the transmitter (0.375 mm away from the transmitter face), where the hologram is located, is calculated using the Fast Nearfield Method (FNM) [15, 16]. FNM is a simulation method that takes advantage of one-dimensional integral approach for rapid calculations of pressure near acoustic sources. The integral is the simplified form of the Rayleigh–Sommerfeld diffraction formula [17] that accounts for a uniform surface velocity of the circular source [18]. To predict the acoustic far-field distribution, we use the Angular Spectrum Approach (ASA) in which the complex acoustic pressure wave is represented as the summation of plane waves [19].

We write

$$p_0(x,y,z=0) = \tilde{p}_0(x,y,z=0)e^{j\Delta\phi(x,y,z)} = \sum_{k_x}\sum_{k_y} P_0(k_x,k_y,z=0)e^{j(k_x x+k_y y+k_z z)} \tag{1}$$

where $\tilde{p}_0$ and $\Delta\phi$ are the amplitude and the relative phase of the complex input acoustic pressure respectively, j is the unit imaginary number and the time dependency of $p_0(x,y,0)$ is excluded for the sake of brevity. In equation (1), k_x and k_y are the transverse wavenumbers that satisfy the Helmholtz equation $\nabla^2 p(\omega) + k^2 p(\omega) = 0$ in the frequency (ω) domain, providing that $k^2 = {k_x}^2 + {k_y}^2 + {k_z}^2$, where $k = \omega/c$ is the wavenumber and c is the speed of sound in a fluid domain. Here, $P_0(k_x,k_y,0)$ is called the angular spectrum of pressure wave at constant $z=0$, which is obtained by the two-dimensional Fourier transform as

$$P_0(k_x,k_y,0) = \int_{-\infty}^{\infty}\int_{-\infty}^{\infty} p_0(x,y,0)e^{-j(k_x x+k_y y)}dxdy. \tag{2}$$

The ASA computes the pressure at any arbitrary plane using pressure field information at a parallel plane, e.g. $z=0$ (such as hologram plane). Hence, when the angular spectrum of input pressure $P_0(k_x,k_y,z=0)$ is identified, the angular spectrum at every parallel plane z is obtained as

$$P(k_x,k_y,z) = P_0(k_x,k_y,0)H(k_x,k_y,z) \tag{3}$$

where $H(k_x,k_y,z)$ is the propagation function [20] written as

$$\begin{aligned} H(k_x,k_y,z) &= e^{jk_z z} \\ k_z &= \sqrt{k^2 - {k_x}^2 - {k_y}^2}. \end{aligned} \tag{4}$$

Accordingly, the pressure distribution at any desired (target) plane z is calculated using the inverse two-dimensional Fourier transform as

$$p(x,y,z) = \frac{1}{4\pi^2}\int_{-\infty}^{\infty}\int_{-\infty}^{\infty} P(k_x,k_y,z)e^{j(k_x x+k_y y)}dk_x dk_y. \tag{5}$$

Similarly, the ASA can be used to compute the backpropagation of the pressure field from the target plane to the hologram plane by

$$P_0(k_x,k_y,0) = P(k_x,k_y,z)H(k_x,k_y,-z) \tag{6}$$

where $H(k_x,k_y,-z)$ is the backpropagation function written as $H(k_x,k_y,-z) = e^{-jk_z z}$.

2.2. Computational method and iterative angular spectrum approach algorithm

To obtain the desired acoustic pressure pattern in the target plane ($z = 50$ mm), the Iterative Angular Spectrum Approach (IASA) [13] is used. The computational domain in the *x*-*y* plane is selected to be at least three times greater than that of the acoustic source dimensions to avoid aliasing of higher spatial frequencies, and then a zero-prescribed field outside the hologram area is applied. The IASA begins by specifying the desired constraints, i.e., boundary conditions in the hologram plane and target plane [10]. Initially, the pressure field in the hologram plane is computed via the FNM near the transmitter, and the phase map is set to zero. In the target plane, after forward-propagated pressure field is calculated via ASA, we impose the desired target image amplitude without any limitations on the phase. Again, the pressure field in the hologram plane is computed via backpropagation of the wave from the target plane to the hologram plane. Then, the acoustic pressure amplitude of the hologram plane is set to that of the initial pressure amplitude close to the transmitter while considering

transmission losses and preserving the back-propagated phase. The transmission coefficient $T(x,y)$ for the normal incident wave is calculated as [21, 22]

$$T(x,y) = 4Z_h^{\,2}Z_0Z_s\left[\left(Z_h^{\,2}+Z_0Z_s\right)^2\sin^2(k_h t(x,y)) + Z_h^{\,2}\left(Z_0+Z_s\right)^2\cos^2(k_h t(x,y))\right]^{-1} \tag{7}$$

where $t(x,y)$ is thickness map of the hologram, k_h is the wave number in the hologram body and Z_h, Z_0 and Z_s are the acoustic impedance of the hologram, medium, and source (transmitter) , respectively. For any material m, the characteristic acoustic impedance is given by $Z_m = \rho_m c_m$, where ρ_m and c_m are the material density and speed of sound, respectively. The thickness map of the hologram neglecting shear waves and attenuation is estimated as

$$\Delta t(x,y) = \frac{\Delta\phi(x,y)}{k_0 - k_h} \tag{8}$$

where $\Delta\phi(x,y)$ is the relative phase map calculated in the hologram plane, $\Delta t(x,y) = t_0 - t(x,y)$, where t_0 is the initial thickness of the hologram plate and k_0 is the wave number in the medium. The IASA is repeated until the acoustic pressure field in the target plane converges to the desired target image, which in turn leads to the convergence of the thickness map of the hologram [10].

2.3. Ultrasonic acoustic energy transfer to multiple 33-mode piezoelectric receivers in the target plane

The receiver disks in the target plane are free-free PZT cylinders operating in the 33-mode of piezoelectricity (3-direction is the axial direction, e.g. ξ-axis, and the longitudinal strain axis and the electrical poling axis are coincident.) with fundamental resonance frequencies above the human audible frequency range (see figure 1). For the fluid-loaded and electrically-loaded free-free piezoelectric receiver disks excited by the acoustic wave, the coupled partial differential equations for longitudinal vibrations of the receivers and the AC electrical circuit equation are given by [6, 14, 23]

$$\begin{aligned} &-YA\frac{\partial^2 u(\xi,t)}{\partial\xi^2} - c_\alpha\frac{\partial^3 u(\xi,t)}{\partial\xi^2\partial t} + c_\beta\frac{\partial u(\xi,t)}{\partial t} + R_r[\delta(\xi)]\frac{\partial u(\xi,t)}{\partial t} + R_r[\delta(\xi-L)]\frac{\partial u(\xi,t)}{\partial t} \\ &+m\frac{\partial^2 u(\xi,t)}{\partial t^2} - \theta v(t)[\delta(\xi-L)-\delta(\xi)] = f_t(t)[\delta(\xi)] - f_b(t-\tau)[\delta(\xi-L)] \end{aligned} \tag{9}$$

$$C_p\frac{dv(t)}{dt} + Y_l v(t) + \int_0^L \theta\frac{\partial^2 u(\xi,t)}{\partial t\partial\xi}d\xi = 0 \tag{10}$$

where $u(\xi,t)$ is the displacement response of the disk at the axial position ξ and time t, $v(t)$ is the voltage output across the electrical load, Y is the Young's modulus at constant electric field, A is the cross-sectional area, m is the mass per unit length, c_α is the stiffness-proportional damping coefficient, c_β is the mass-proportional damping coefficient, θ is the electromechanical coupling term in physical coordinates, and $\delta(\xi)$ is the Dirac delta function. Furthermore, in equation (10), C_p and $Y_l = 1/R_l$, where R_l is the load resistance, are the internal capacitance of the piezoelectric receivers and the admittance of the external load, respectively. The excitation forces due to the incident acoustic pressure are $f_t(t) = p_i(t)A$ at $\xi = 0$ and $f_b(t-\tau) = \mu p_i(t-\tau)A$ at $\xi = L$, given in terms of the acoustic pressure in the target plane $p(t)$ (see section 2.2) evaluated at the top surface $(\xi = 0)$ and the bottom surface $(\xi = L)$ of the receivers, where μ is the ratio of the acoustic pressure on the bottom surface to that on the top surface and τ is the time delay of f_b relative to f_t . Moreover, the dissipative term R_r in equation (9) is the resistive component of the fluid radiation impedance (see figure 10.19 in [24]). The mass normalized elastic-mode eigenfunction, calculated from the corresponding undamped and electromechanically uncoupled (short-circuit) free vibration, is obtained as [6]

$$\phi(\xi)=\frac{\cos(\alpha\xi/L)-\alpha\frac{m_r}{mL}\sin(\alpha\xi/L)}{\sqrt{\int_0^L m\left(\cos(\alpha\xi/L)-\alpha\frac{m_r}{mL}\sin(\alpha\xi/L)\right)^2 d\xi+m_r\left(\cos(\alpha)-\alpha\frac{m_r}{mL}\sin(\alpha)\right)^2+m_r}} \tag{11}$$

where the eigenvalue (α) of the fundamental mode is the first non-zero root of the transcendental equation $[\alpha^2(\frac{m_r}{mL})^2-1]\sin\alpha-2\alpha\frac{m_r}{mL}\cos(\alpha)=0$, where $m_r=X_r/\omega$ is the radiation mass, i.e., added mass, due to reactive component of fluid radiation impedance X_r (see figure 10.19 in [24]) and ω is the excitation frequency.

The electromechanically coupled equations of forced vibrations and current balance are expressed for the fundamental mode in lumped-parameter form as

$$\ddot{x}(t)+\left[2\zeta\omega_n+R_r\phi^2(0)+R_r\phi^2(L)\right]\dot{x}(t)+\omega_n^2x(t)-\theta[\phi(0)\phi(L)-\phi^2(0)]v(t)=f_t(t)\phi^2(0)-f_b(t-\tau)\phi(0)\phi(L) \tag{12}$$

$$C_p\phi(0)\dot{v}(t)+Y_l\phi(0)v(t)+\theta[\phi(L)-\phi(0)]\dot{x}(t)=0 \tag{13}$$

where an over-dot represents differentiation with respect to time.

The steady-state electromechanical response to harmonic excitation force $f(t)=Fe^{j\omega t}$ is also harmonic and is of the form $x(t)=Xe^{j\omega t}$ and $v(t)=Ve^{j\omega t}$ based on the linear system assumption. As a result, the fundamental-mode output voltage amplitude frequency response function (FRF) is obtained as [6]

$$V=\frac{j\omega\theta F\left(\phi(0)-\mu\phi(L)e^{-j\varphi}\right)\left(\phi(0)-\phi(L)\right)}{\left\{\omega_n^2-\omega^2+j\omega\left[2\zeta\omega_n+R_r\left(\phi^2(0)+\phi^2(L)\right)\right]\right\}\left(Y_l(\omega)+j\omega C_p\right)+j\omega\theta^2\left(\phi(L)-\phi(0)\right)^2} \tag{14}$$

where $\varphi=\omega\tau$ is the phase angle between the excitation forces at the top and bottom surfaces of the cylindrical receivers. The power output FRF of the piezoelectric receiver disks (Π) is calculated using equation $\Pi=v^2/R_l$.

Deriving an expression for the impedance of the fluid-loaded receivers is useful for identification of its parameters such as underwater short- and open-circuit natural frequencies ω_n under electrical excitation. In equation (12), changing the input to $v(t)=Ve^{j\omega t}$ and setting $f_t(t)=f_b(t-\tau)=0$, while in equation (13), replacing the current output $Y_lv(t)$ by the actuation current input $-i(t)=-Ie^{j\omega t}$, yields

$$Z(\omega)=\frac{1}{j\omega\left[C_p+\frac{\theta^2[\phi(L)-\phi(0)]^2}{\omega_n^2-\omega^2+j\omega\left[2\zeta\omega_n+R_r\phi^2(0)+R_r\phi^2(L)\right]}\right]} \tag{15}$$

for the fluid-loaded receivers' electromechanical impedance ($Z=V/I$), which includes the fundamental longitudinal vibration mode only.

3. COMPUTATIONAL RESULTS

3.1. Acoustic pressure field in the target plane and the thickness map of the hologram

Having computed the initial pressure field close to the face of the circular transmitter using the FNM at 1 MHz, the ASA is used to compute the pressure field in the target plane at $z = 50$ mm. Figure 2a shows the pressure distribution in the target plane when there is no hologram. On the other hand, the IASA algorithm is applied to propagate the pressure field from the hologram plane to the target plane, which converges to the target image after several iterations. Figure 2b shows the pressure distribution in the target plane after 50 iterations (in the presence of the hologram located close to the transmitter). The resultant acoustic pressure pattern matches well with the desired pattern that we imposed upon the target plane (VT shape pattern). It shows the capability of the designed hologram in multi-focal lensing and acoustic pressure transmission, which generates higher amplitudes in the area of the desired pattern in the target plane (about 32% increase in total acoustic pressure). As explained earlier in the theory section, the back-propagated final pressure distribution in the hologram plane is then used to compute the final thickness map of the hologram using the final calculated relative phase map. Figure 2c illustrates the final thickness map, which is later used as an input to the 3D printer for the hologram fabrication (figure 2d). The hologram is printed with a 3D printer (Form 2, Formlabs) with a resolution of 50 µm. The quality or the resolution of the 3D-printed hologram will be tested in future work, for the application of acoustic power transmission.

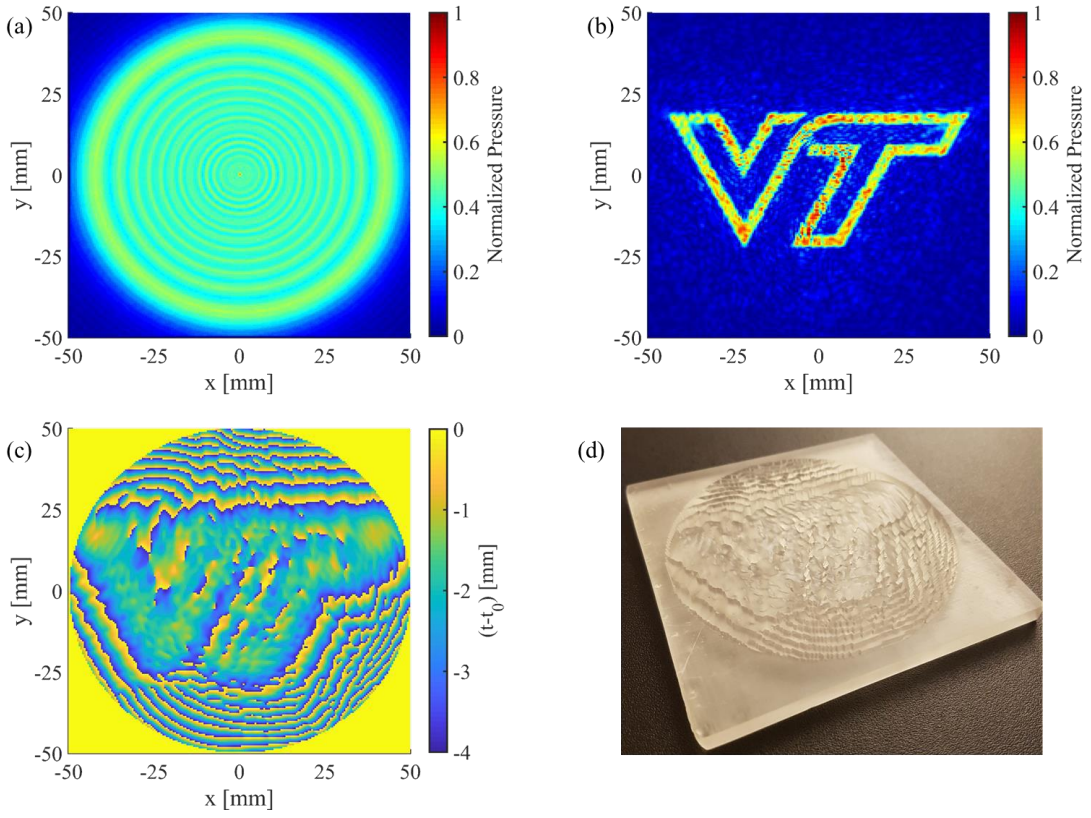

Figure 2. Acoustic pressure distribution in the target plane at $z = 50$ mm (a) when there is no hologram and (b) in the presence of the hologram. (c) Final thickness map of the hologram plate obtained from the IASA and (d) the 3D-printed hologram plate.

3.2. Electromechanical impedance and receivers' power output in the target plane

Having obtained the pressure distribution in the target plane (figure 2b) where 1024 PZT receivers are equally distributed in an area of 100 cm^2, the receivers' power output in the target plane is calculated using equation $\Pi = v^2 / R_l$ and shown in figure 4. Each receiver investigated in this case study is a cylindrical 33-mode PZT disk (PIC 255 from Physik

Instrumente (PI) GmbH & Co. KG [25]) with a diameter of 3 mm and thickness of 2 mm, and a short-circuit fundamental resonance frequency of 1 MHz in free-free boundary conditions. The material properties are given by the manufacturer [26]. The whole setup (in figure 1) is submerged under water. The analytical impedance FRFs for in-air and underwater actuation are shown in figure 3 as obtained from equation 15. The impedance curves capture the fundamental resonance and anti-resonance frequencies of the receiver disk, which are also called the short- and open-circuit resonance frequencies, and they have the values of 1 and 1.08 MHz, respectively. The effects of the added mass and damping due to water loading are clearly observed in figure 3, and the model successfully represents the underwater dynamics of the receiver near resonance. It should be noted that the resistive and reactive components of the radiation impedance determine the fluid-induced damping and fluid-loaded resonance frequency, and they depend on the diameter of the receiver.

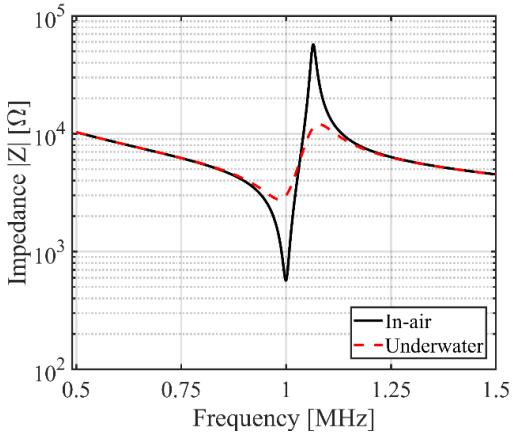

Figure 3. In-air and underwater electromechanical impedance FRFs of the piezoelectric receiver disk in free-free boundary conditions.

Using the analytical model, further simulations are conducted to obtain the electrical power output for the PZT receivers in the target plane at $z = 50$ mm for two cases, where there is no acoustic hologram and in the presence of the hologram at 1.08 MHz; the underwater open-circuit resonance frequency, and the load resistance is fixed to $R_l = 12\,\mathrm{k}\Omega$. The pressure amplitude in the target plane at each receiver's location is used to calculate the external force acting on the surfaces of the receiver and is used in equation (14) to compute the output voltage amplitude from each receiver. This voltage is used in conjunction with the electrical load to calculate the power output. Since the pressure distribution over the surface of each receiver is not uniform, the pressure field in the target plane is divided into a coarser grid that has the nominal dimension of the diameter of the receivers. The pressure over each grid point is then averaged and is multiplied by the receiver area to estimate the external force over each receiver's top surface.

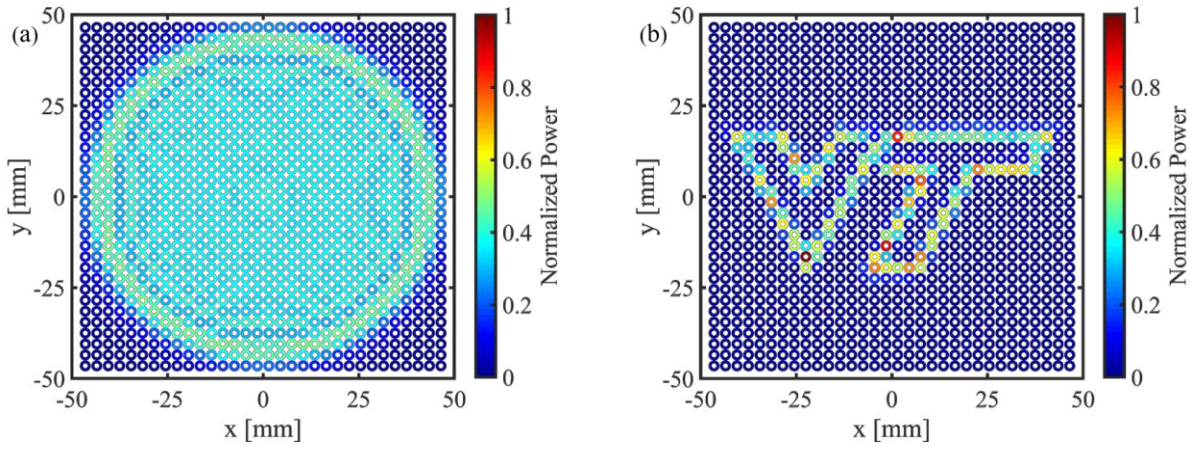

Figure 4. Power output for the piezoelectric receivers in the target plane at $z = 50$ mm (a) when there is no hologram and (b) in the presence of the hologram.

Figure 4 shows an array of receivers that covers the domain in the target plane corresponding to the hologram aperture. The power output without the presence of the hologram is shown in figure 4a, while figure 4b shows the power output using the acoustic hologram. It is shown that the acoustic hologram enables a new capability in shaping the acoustic pressure field and transferring power to the receivers only at focal points (receivers located in the VT pressure pattern), selectively. For this case study, in addition to pattering, employing the hologram in the UAET setup leads to a 9% increase in the total power output. Furthermore, the receiver with the highest power output (in figure 4b) has a 200% increase in comparison to the receiver in the same location without the placement of the hologram. The power can be further increased with impedance mismatch alleviation and the inclusion of impedance-matching layers between the transmitter, hologram and receivers [22].

4. CONCLUSIONS

Contactless acoustic energy transfer has many applications ranging from wireless charging of deep medical implants to sensor networks. Patterning and focusing of the transmitted acoustic energy in space is one of the challenges for locally charging sensors and devices. UAET can be used in conjunction with acoustic holograms to shape (pattern) the acoustic pressure field in a target plane and accomplish energy localization. In this paper, an iterative angular spectrum approach is used to design an acoustic hologram for constructing a multi-focal pressure pattern which leads to power focusing. The wavefront pressure distribution is used as an input to the fundamental-mode output voltage amplitude equation derived from a distributed-parameter model to compute the power output from an array of piezoelectric receivers located in a desired pattern. The results show that combining metamaterial-based holograms with UAET allows for the selective transfer of energy using the advantages of beam steering and multi-focal lensing. Future research directions of this project include experimental validations of the mathematical model to investigate the transmitted power efficiency and patterning using acoustic holograms.

5. ACKNOWLEDGEMENT

This work was supported in part by the NSF Grant ECCS-1711139, which is gratefully acknowledged.

REFERENCES

[1]. Roes, M.G., et al., "*Acoustic energy transfer: A review*". IEEE Transactions on Industrial Electronics, 2013. **60**(1): p. 242-248.

[2]. Yoshizawa, S., et al., "*High intensity focused ultrasound lithotripsy with cavitating microbubbles*". Medical & biological engineering & computing, 2009. **47**(8): p. 851-860.

[3]. Akyildiz, I.F., et al., "*Wireless sensor networks: a survey*". Computer networks, 2002. **38**(4): p. 393-422.

[4]. Seo, D., et al., "*Model validation of untethered, ultrasonic neural dust motes for cortical recording*". Journal of neuroscience methods, 2015. **244**: p. 114-122.

[5]. ter Haar, G. and C. Coussios, "*High intensity focused ultrasound: physical principles and devices*". International Journal of Hyperthermia, 2007. **23**(2): p. 89-104.

[6]. Shahab, S., M. Gray, and A. Erturk, "*Ultrasonic power transfer from a spherical acoustic wave source to a free-free piezoelectric receiver: Modeling and experiment*". Journal of Applied Physics, 2015. **117**(10): p. 104903.

[7]. Carrara, M., et al., "*Dramatic enhancement of structure-borne wave energy harvesting using an elliptical acoustic mirror*". Applied Physics Letters, 2012. **100**(20): p. 204105.

[8]. Carrara, M., et al., "*Fourier transform-based design of a patterned piezoelectric energy harvester integrated with an elastoacoustic mirror*". Applied Physics Letters, 2015. **106**(1): p. 013907.

[9]. Shmilovitz, D., et al., "*Noninvasive control of the power transferred to an implanted device by an ultrasonic transcutaneous energy transfer link*". IEEE Transactions on Biomedical Engineering, 2014. **61**(4): p. 995-1004.

[10]. Melde, K., et al., "*Holograms for acoustics*". Nature, 2016. **537**(7621): p. 518.

[11]. Xie, Y., et al., "*Acoustic holographic rendering with two-dimensional metamaterial-based passive phased array*". Scientific reports, 2016. **6**: p. 35437.

[12]. Dunn, F., et al., [*Springer handbook of acoustics*]. 2015: Springer.

[13]. Mellin, S.D. and G.P. Nordin, "*Limits of scalar diffraction theory and an iterative angular spectrum algorithm for finite aperture diffractive optical element design*". Optics Express, 2001. **8**(13): p. 705-722.

[14]. Shahab, S. and A. Erturk, "*Contactless ultrasonic energy transfer for wireless systems: acoustic-piezoelectric structure interaction modeling and performance enhancement*". Smart Materials and Structures, 2014. **23**(12): p. 125032.

[15]. McGough, R.J., "*Rapid calculations of time-harmonic nearfield pressures produced by rectangular pistons*". The Journal of the Acoustical Society of America, 2004. **115**(5): p. 1934-1941.

[16]. Zeng, X. and R.J. McGough, "*Evaluation of the angular spectrum approach for simulations of near-field pressures*". The Journal of the Acoustical Society of America, 2008. **123**(1): p. 68-76.

[17]. Goodman, J.W., [*Introduction to Fourier optics*]. 2005: Roberts and Company Publishers.

[18]. Kelly, J.F. and R.J. McGough, "*A time-space decomposition method for calculating the nearfield pressure generated by a pulsed circular piston*". IEEE transactions on ultrasonics, ferroelectrics, and frequency control, 2006. **53**(6): p. 1150-1159.

[19]. Williams, E.G., [*Fourier acoustics: sound radiation and nearfield acoustical holography*]. 1999: Academic press.

[20]. Liu, D.-L. and R.C. Waag, "*Propagation and backpropagation for ultrasonic wavefront design*". IEEE transactions on ultrasonics, ferroelectrics, and frequency control, 1997. **44**(1): p. 1-13.

[21]. Lawrence, E.K., et al., "*Fundamentals of acoustics*". New yorks: John wileys, c2000, 2000: p. 169-151.

[22]. Callens, D., C. Bruneel, and J. Assaad, "*Matching ultrasonic transducer using two matching layers where one of them is glue*". Ndt & E International, 2004. **37**(8): p. 591-596.

[23]. Shahab, S., M. Gray, and A. Erturk. *An experimentally validated contactless acoustic energy transfer model with resistive-reactive electrical loading*. in *Active and Passive Smart Structures and Integrated Systems 2015*. 2015. International Society for Optics and Photonics.

[24]. Butler, J.L. and C.H. Sherman, [*Transducers and arrays for underwater sound*]. 2016: Springer.

[25]. https://www.piceramic.com/en/company/.

[26]. https://www.piceramic.com/en/products/piezoceramic-materials/.